Uncertainty analysis for the integration of seismic and CSEM data

Myoung Jae Kwon & Roel Snieder
Center for Wave Phenomena, Colorado School of Mines

ABSTRACT

Geophysical inverse problems consist of three stages: the forward problem, optimization, and appraisal. We study the appraisal problem for the joint inversion of seismic and controlled source electro-magnetic (CSEM) data and utilize rock-physics models to integrate these two disparate data sets. The appraisal problem is solved by adopting a Bayesian model and we incorporate four representative sources of uncertainty. These are uncertainties in (1) seismic wave velocity, (2) electric conductivity, (3) seismic data, and (4) CSEM data. The uncertainties in porosity and water saturation are quantified by a posterior random sampling in the model space of porosity and water saturation of a marine one-dimensional structure. We study the relative contributions from the four individual sources of uncertainty by performing several statistical experiments. The uncertainties in the seismic wave velocity and electric conductivity play a more significant role on the variation of posterior uncertainty than do the seismic and CSEM data noise. The numerical simulations also show that the assessment of porosity is most affected by the uncertainty in seismic wave velocity and the assessment of water saturation is most influenced by the uncertainty in electric conductivity. The framework of the uncertainty analysis presented in this study can be utilized to effectively reduce the uncertainty of the porosity and water saturation derived from integration of seismic and CSEM data.

Key words: uncertainty analysis, Metropolis-Hastings algorithm, CSEM

1 INTRODUCTION

Currently, there is an increasing interest in the integration of the seismic and controlled source electromagnetic (CSEM) method in deep marine exploration (Harris & MacGregor, 2006). Although the CSEM method has less resolution than the seismic method, it provides extra information about, for example, electric conductivity. This property is important for the economic evaluation of reservoirs. Therefore, the CSEM method is considered an effective complementary tool when combined with seismic exploration.

The seismic and CSEM methods are disparate exploration techniques that are sensitive to different medium properties: the seismic method is sensitive to density and seismic wave velocity and the CSEM method to electric conductivity. There have been several approaches for joint inversion that integrate disparate data sets. Some of them assume a common structure (Musil *et al.*, 2003) or similar structural variations of different medium properties (Gallardo & Meju, 2004). More recently, the application of rock-physics models for joint inversion has been studied (Hoversten *et al.*, 2006). Rock-physics models enable us to interrelate seismic wave velocity and electric conductivity with the reservoir parameters such as porosity, water saturation, or permeability. The main advantage of the approach is that the reservoir parameters have great economic importance. The application of a rock-physics model is limited, however, by the fact that such a model is site-specific and there are not yet any universal solutions to the inverse problem. Furthermore, even for any particular area of interest, any rock-physics model is generally described as a cloud of samples. These limitations

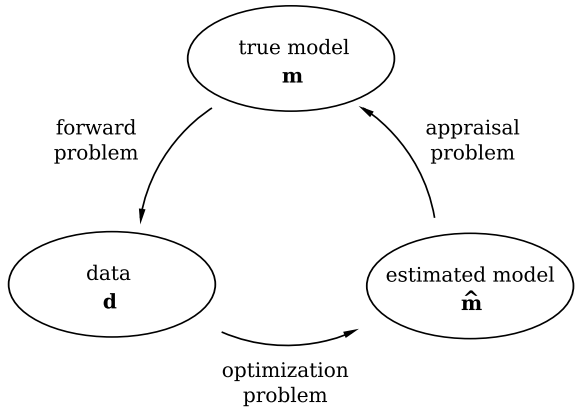

Figure 1. Division of an inverse problem into a forward problem, an optimization problem, and an appraisal problem.

imply that joint inversion via a rock-physics model intrinsically necessitates a stochastic approach. Stochastic inversion has recently been studied for seismic inversion (Spikes *et al.*, 2007) and joint inversion of seismic and CSEM data (Chen *et al.*, 2007). However, the contributions of rock-physics model uncertainties are not yet well understood. In fact, the accuracy of our joint inversion is limited by the uncertainty of rock-physics model as well as by the data noise. We therefore model both the data noise and the uncertainty of rock-physics models in this research.

In many geophysical inverse problems, we have finite data and retrieve a model that has infinitely many degrees of freedom (Snieder, 1998). So far, most of the geophysical inversion studies have concentrated on finding the model that best fits the data; this is an optimization problem. In this research we quantify how much confidence we can place in the optimum solution; this is an appraisal problem. The appraisal problem has particular significance when the rock-physics model is used for the joint inversion of the seismic and CSEM data. We investigate the relative contribution of different sources of overall uncertainty that arise when we use rock-physics models for the joint inversion. These include seismic data noise, CSEM data noise, and uncertainties of rock-physics models. We implement several numerical experiments that reflect scenarios we may encounter in practice and compare the uncertainties in the inferred parameters. The comparison reveals the relative contributions of different sources of uncertainty and we can utilize the procedure to more effectively reduce the uncertainty, depending on whether our interests focus on porosity or water saturation.

2 METHODOLOGY

The goal of geophysical inversion is to make quantitative inferences about the earth from noisy data. There are mainly two different approaches for attaining this goal: in one the unknown models are assumed deterministic and one uses inversion methods such as Tikhonov regularization; in the other all the unknowns are random and one uses Bayesian methods. The object of this project is to provide a framework for Bayesian joint inversion that leads to model estimates and their uncertainties.

The connection between geophysical data $\mathbf{d}$ and model $\mathbf{m}$ is written as

$$\mathbf{d} = L[\mathbf{m}] + \mathbf{e} \tag{1}$$

where L denotes a linear or nonlinear operator that maps the model into the data and $\mathbf{e}$ represents data measurement error. The details of the operator are presented in the modeling procedure section. Bayes' theorem relates conditional and marginal probabilities of a data $\mathbf{d}$ and a model $\mathbf{m}$ as follows (Scales & Snieder, 1997; Sivia & Webster, 1998):

$$\pi(\mathbf{m}|\mathbf{d}) = \frac{\pi(\mathbf{m})f(\mathbf{d}|\mathbf{m})}{\pi(\mathbf{d})} \propto \pi(\mathbf{m})f(\mathbf{d}|\mathbf{m}), \tag{2}$$

where $\pi(\mathbf{m})$ is a prior probability in the sense that it does not take into account any information about the data $\mathbf{d}$; $f(\mathbf{d}|\mathbf{m})$ is likelihood of the data $\mathbf{d}$, given a model $\mathbf{m}$; and $\pi(\mathbf{m}|\mathbf{d})$ is a posterior probability density that we are inferring. The denominator of equation (2) is the probability distribution of the data $\mathbf{d}$. This quantity can be written as $\pi(\mathbf{d}) = \int \pi(\mathbf{m})f(\mathbf{d}|\mathbf{m})\, d\mathbf{m}$. In practical applications, the denominator is not evaluated and the relative change of the posterior probability as a function of the model parameter is investigated.

2.1 Hierarchical Bayesian model

The P-wave velocity and electric conductivity are derived from two reservoir parameters: porosity and water saturation. These reservoir parameters are the target model parameters in this project. There are two layers of likelihood probabilities that have hierarchical dependency. The variables and their hierarchical dependencies are displayed in Figure 2. The uppermost row represents prior probabilities of the reservoir parameters: the porosity ($\mathbf{m}_\phi$) and water saturation ($\mathbf{m}_{S_w}$). The middle row denotes the likelihoods of the P-wave velocity ($\mathbf{d}_{Vp}$) and logarithm of electric conductivity ($\mathbf{d}_{\sigma_e}$). Finally, the lowermost row represents the likelihoods of the seismic ($\mathbf{d}_s$) and CSEM data ($\mathbf{d}_e$).

Within the Bayesian framework, the prior probabilities of the reservoir parameters are expressed as $\pi(\mathbf{m}_\phi)$ and $\pi(\mathbf{m}_{S_w})$. Likewise, four possible likelihoods are expressed as follows: the likelihoods of the P-wave velocity $f(\mathbf{d}_{V_p}|\mathbf{m}_\phi, \mathbf{m}_{S_w})$, logarithm of electric conductivity $f(\mathbf{d}_{\sigma_e}|\mathbf{m}_\phi, \mathbf{m}_{S_w})$, seismic data $f(\mathbf{d}_s|\mathbf{d}_{V_p})$, and CSEM data $f(\mathbf{d}_e|\mathbf{d}_{\sigma_e})$. Therefore, the posterior probabilities (π_{post}) of the porosity and water saturation are derived from the prior (π_{prior}) and likelihood probabilities (f)

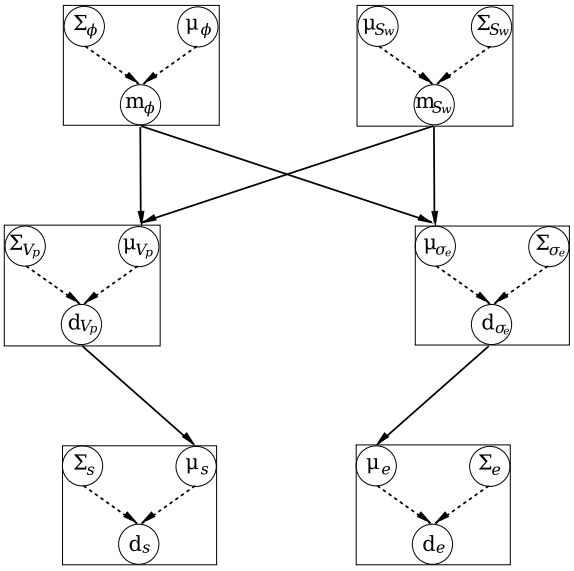

Figure 2. A hierarchical dependency structure represented by a directed graph. The nodes represent stochastic variables, the dashed arrows represent probability dependencies, and the solid arrows represent deterministic relationships. μ and $\mathbf{\Sigma}$ denote expectation vectors and covariance matrices, respectively. $\mathbf{m}_\phi$ and $\mathbf{m}_{S_w}$ represent two reservoir parameters: medium porosity and water saturation. $\mathbf{d}_{V_p}$ and $\mathbf{d}_{\sigma_e}$ denote P-wave velocity and logarithm of electric conductivity, respectively. $\mathbf{d}_s$ and $\mathbf{d}_e$ represent two different data sets: seismic and CSEM data.

as follows:

$$\begin{aligned} & \pi_{post}(\mathbf{m}_\phi, \mathbf{m}_{S_w}|\mathbf{d}_{V_p}, \mathbf{d}_{\sigma_e}, \mathbf{d}_s, \mathbf{d}_e) \\ \propto\ & \pi(\mathbf{m}_\phi, \mathbf{m}_{S_w}, \mathbf{d}_{Vp}, \mathbf{d}_{\sigma_e}, \mathbf{d}_s, \mathbf{d}_e) \\ =\ & \pi_{prior}(\mathbf{m}_\phi)\pi_{prior}(\mathbf{m}_{S_w}) \\ \times\ & f(\mathbf{d}_{V_p}|\mathbf{m}_\phi, \mathbf{m}_{Sw}) f(\mathbf{d}_{\sigma_e}|\mathbf{m}_\phi, \mathbf{m}_{Sw}) \\ \times\ & f(\mathbf{d}_s|\mathbf{d}_{Vp}) f(\mathbf{d}_e|\mathbf{d}_{\sigma_e}). \end{aligned} \quad (3)$$

Equation (3) indicates that the posterior probability is proportional to the product of individual priors and likelihoods.

In statistics, the central limit theorem states that the sum of a sufficiently large number of identically distributed independent random variables follow a normal distribution. This implies that the normal distribution is a reasonable choice for describing probability. Therefore, throughout this project, we assume the priors and likelihoods to follow multivariate Gaussian distribution with expectation vector μ and covariance matrix $\mathbf{\Sigma}$, such that

$$f(\mathbf{x}) = \frac{1}{\sqrt{(2\pi)^n |\mathbf{\Sigma}|}} \exp\left[-\frac{1}{2}(\mathbf{x}-\mu)^T \mathbf{\Sigma}^{-1}(\mathbf{x}-\mu)\right], \quad (4)$$

where $\mathbf{x}$ denotes data or model and n denotes the dimension of $\mathbf{x}$. The covariance matrix is modeled as a diagonal matrix as follows:

$$\mathbf{\Sigma} = \text{diag}\ \{\sigma_1^2, \sigma_2^2, \cdots, \sigma_n^2\}, \quad (5)$$

where σ_i^2 denote the variance value of a datum or model parameter. If the error structure is apparently different from Gaussian, another appropriate probability function should be modeled. Equation (4) expresses the general form of the probability function used in this project and the covariance matrices for individual prior and likelihoods are discussed later. Note that since the forward operations in this project (solid arrows in Figure 2) are nonlinear, the posterior distributions are not necessarily Gaussian.

2.2 Prior and likelihood model

In the Bayesian context, there are several approaches to represent prior information (Scales & Tenorio, 2001). The prior model encompasses all the information we have before the data sets are acquired. In practice, the prior information includes the definition of the model parameters, geologic information about the investigation area, and preliminary investigation results. Therefore, the prior model is the starting point of a Bayesian approach, and we expect to have a posterior probability distribution with less uncertainty than the prior probability. The prior model also plays an important role in Bayesian inversion to eliminate unreasonable models that fit the data (Tenorio, 2001). Obvious prior information we have is the definition of the porosity and water saturation, such that $0 \leq m_{\phi_i} \leq 1$ and $0 \leq m_{S_{w_i}} \leq 1$. This implies that the prior distributions of the porosity and water saturation are intrinsically non-Gaussian. However, when the variances of the distributions are sufficiently small, the deviation from the Gaussian approximation is negligible. We adopt this assumption and take the Gaussian approximations for the modeling of the prior probabilities. We further assume that the covariance matrices $\mathbf{\Sigma}_\phi$ and $\mathbf{\Sigma}_{S_w}$ (Figure 2) are diagonal and that the diagonal elements within each covariance matrix are identical.

For the hierarchical Bayesian model shown in Figure 2, there are four elementary likelihoods. Each of these likelihoods describes how well any rock-physics model or geophysical forward modeling fits with the rock-physics experiment results or the noisy observations. The details of the likelihood modeling are covered in the modeling procedure section.

2.3 MCMC sampling

The assessment of the posterior probability requires great computational resources and, in most cases, it is still impractical for 3-D inverse problems. Pioneering studies about the assessment were performed for 1-D seismic waveform inversion (Gouveia & Scales, 1998; Mosegaard *et al.*, 1997). The posterior model space of this project encompasses porosity and water saturation of several layers. We use a Markov-Chain Monte Carlo

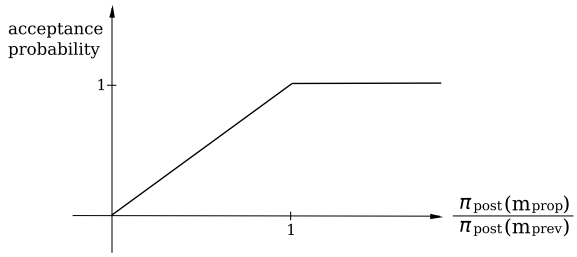

Figure 3. Acceptance probability as a function of the posterior probability ratio between the previous and proposal sample.

(MCMC) sampling method (Kaipio *et al.*, 2000) to indirectly estimate the posterior probability distribution of the porosity and water saturation. In this project, the goal of the MCMC sampling method is to retrieve a set of samples, such that the sample distribution describes the joint posterior probability of equation (3). The MCMC sampling method is a useful tool to explore the space of feasible solutions and to investigate the resolution or uncertainty of the solution (Mosegaard & Sambridge, 2002; Sambridge *et al.*, 2006). The Metropolis-Hastings algorithm (Hastings, 1970; Metropolis *et al.*, 1953) and Gibbs sampler (Geman & Geman, 1984) are the most widely used samplers for this purpose. We apply the Metropolis-Hastings algorithm for the assessment of posterior probability.

The Metropolis-Hastings algorithm is a method for generating a sequence of samples from a probability distribution that is difficult to sample directly. The actual implementation of the algorithm is comprised of the following steps (Kaipio *et al.*, 2000).

(i) Pick an initial sample $\mathbf{m}_{prev} \in \mathbb{R}^n$ and set $k = 1$, $\mathbf{m}^{(k)} = \mathbf{m}_{prev}$.
(ii) Increase $k \rightarrow k + 1$.
(iii) Draw a proposal sample $\mathbf{m}_{prop} \in \mathbb{R}^n$ from the proposal distribution $q(\mathbf{m}_{prev}, \mathbf{m}_{prop})$ and calculate the acceptance ratio

$$\alpha(\mathbf{m}_{prev}, \mathbf{m}_{prop}) = \min\left[1, \frac{\pi_{post}(\mathbf{m}_{prop})}{\pi_{post}(\mathbf{m}_{prev})}\right]. \quad (6)$$

(iv) Draw $t \in [0, 1]$ from uniform probability density.
(v) If $\alpha(\mathbf{m}_{prev}, \mathbf{m}_{prop}) \geq t$, set $\mathbf{m}^{(k)} = \mathbf{m}_{prop}$, else $\mathbf{m}^{(k)} = \mathbf{m}_{prev}$.
(vi) When k is the desired sample size, stop, or else, repeat starting from step (ii).

Figure 3 shows the acceptance probability of the Metropolis-Hastings algorithm as a function of the posterior probability ratio between the previous and proposal sample. Note that regardless of how small the posterior probability ratio is, there always is a certain probability of accepting the proposal sample. We choose a Gaussian distribution as a proposal distribution as follows:

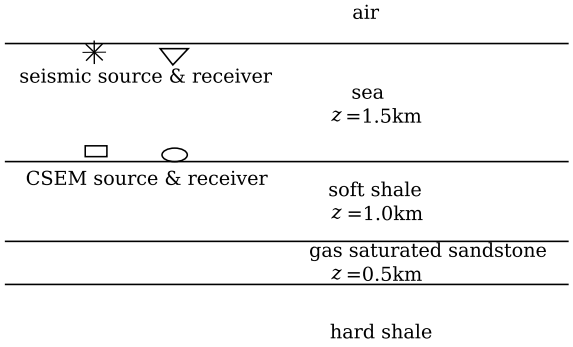

Figure 4. Cartoon of the employed marine 1-D model. Seismic source and receiver are located 10 m below the sea surface. CSEM source is located 1 m above the sea bottom and receiver is on the bottom. The earth is modeled as four homogeneous isotropic layers: seawater, soft shale, gas saturated sandstone, and hard shale. The air and hard shale layer are the two infinite half-spaces. The thicknesses (z) of the layers between the two half-spaces are fixed.

$$\mathbf{m}_{prop} \sim N(\mathbf{m}_{prev}, \sigma_i^2 \mathbf{I}), \quad (7)$$

where the variances σ_i^2 describe the probabilistic sampling step of the model parameters during the random simulation. If σ_i^2 is too big, the drawn $\mathbf{m}_{prop}$ is practically never accepted. On the other hand, if σ_i^2 is too small, a proper sampling of the distribution requires a prohibitively large sample set. A good rule of thumb is that of all $\mathbf{m}_{prop}$, roughly 20 - 30% should be accepted (Kaipio *et al.*, 2000).

3 MODELING PROCEDURES

The marine 1-D model used in this research is shown in Figure 4. The target layer, a gas saturated sandstone layer, is located between shale layers above and below. The soft shale layer is modeled to have the highest clay content and the gas saturated sandstone layer to have the lowest clay content. The ground truth values of the porosities ϕ, water saturations S_w, P-wave velocities V_p and electric conductivities σ_e are summarized in Table 1. The mean prior porosity μ_ϕ and water saturation μ_{S_w} values are assumed to be the ground truths.

3.1 Rock-physics likelihood modeling

Rock-physics models play a central role in the joint inversion presented here. However, the rock-physics models are in many cases site-specific and complicated functions of many variables. Therefore, we utilize several empirical relations that are widely accepted. The bulk modulus K is a function of porosity ϕ and water saturation S_w. For a fluid-saturated medium, the bulk modulus is given by Gassmann's equation (Han & Batzle,

	ϕ (%)	S_w (%)	V_p (km/s)	σ_e (S/m)
soft shale layer	35	90	2.30	0.430
gas saturated sandstone layer	25	10	3.57	0.003
hard shale layer	10	50	4.86	0.018

Table 1. Ground truth values of the porosities ϕ, water saturations S_w, P-wave velocities V_p, and electric conductivities σ_e of the 1-D model shown in Figure 4.

clay mineral	CEC (coulomb/kg)
kaolinite	2,000 - 10,000
illite	10,000 - 38,000
montmorillonite	67,000 - 77,000
smectite	77,000 - 144,000

Table 2. Typical ranges of the cation exchange capacity (CEC) value for authigenic forms of the clay minerals.

2004) as follows:

$$K = K_d + \frac{(1 - \frac{K_d}{K_0})^2}{\frac{\phi}{K_f} + \frac{1-\phi}{K_0} - \frac{K_d}{K_0^2}}, \tag{8}$$

where K_d, K_0, and K_f are the bulk modulus of the dry rock, mineral material, and pore fluid, respectively. We model two phases of pore fluid: water and gas. A mixture of two different pore fluids can be regarded as an effective fluid model and the bulk modulus is derived from Wood's equation (Batzle & Wang, 1992) as follows:

$$\frac{1}{K_f} = \frac{S_w}{K_w} + \frac{1 - S_w}{K_g}, \tag{9}$$

where K_w and K_g are the bulk modulus of the water and gas phase. One more factor that has significant effect on the P-wave velocity of a medium is the clay content. Han's empirical relations (Mavko *et al.*, 1998) state that the clay content c reduces the P-wave velocity. Applying a Han's empirical relation, we derive the P-wave velocity as

$$V_p = \sqrt{\frac{K + \frac{4}{3}\mu}{\rho}} - 2.18c \text{ km/s}, \tag{10}$$

where the bulk modulus K and shear modulus μ are in GPa and density ρ is in g/cc. In this project, the clay contents are assumed to be constant (20%, 1%, and 10% for the soft shale, sandstone, and hard shale layer, respectively).

The relationship between the reservoir parameters (porosity ϕ and water saturation S_w) and electric conductivity is given by Archie's second law (Mavko *et al.*, 1998), which describes the electric conductivity in clean sands. The electric conductivity in shaley sands is complicated by the presence of clays and is described by Waxman-Smits formula (Revil *et al.*, 1998; Waxman & Smits, 1968):

$$\sigma_e = \phi^m S_w^n \left[\sigma_w + \frac{BQ_v}{S_w}\right], \tag{11}$$

where m is cementation exponent, n is saturation exponent, and σ_w is electric conductivity of pore fluid. Empirically, the cementation and saturation exponents are close to 2 for most sedimentary rocks (Mavko *et al.*, 1998), and this value is used in this project. The parameter B is an equivalent counterion mobility and Q_v is the excess of surface charge per unit pore volume. The parameter B is given empirically at 25°C by

$$B = B_0 \left[1 - 0.6 \exp\left(-\frac{\sigma_w}{0.0013}\right)\right], \tag{12}$$

where σ_w is in S/m and the maximum counterion mobility B_0 is given by 4.78×10^{-8} m^2/volt/s (Revil *et al.*, 1998). The parameter Q_v is related to the grain density ρ_g (in kg/m^3) and the cation exchange capacity (CEC) (Waxman & Smits, 1968) by

$$Q_v = \rho_g \frac{1 - \phi}{\phi} \text{CEC}. \tag{13}$$

The CEC is usually significant only for clay minerals and the vaules for the representative clay minerals are shown in Table 2. As is indicated in the table, the variation of the CEC for the different clay mineral is dramatic. For a mixture of sand grains and clay minerals, the CEC of the sediment is calculated by

$$\text{CEC} = f_c \sum_i \chi_i \text{ CEC}_i, \tag{14}$$

where f_c is the mass fraction of clay minerals, χ_i are the relative fractions of each clay minerals in the shale fraction, and CEC_i is the cation exchange capacity of each of these clay minerals. Because of the large grain size, the CEC of the quartz grains can be neglected. In this project, we simplify the contribution of the clay contents on the electric conductivity and assume that the clay content in the shale fraction is only composed of kaolinite.

We assume that the distribution of P-wave velocity follows a Gaussian distribution. In contrast, considering that the electric conductivity exhibits exponential variation in most geologic environments, we assume that the electric conductivity follows a lognormal distribution. The P-wave velocity and electric conductivity are derived from equations (10) - (11), and Gaussian and

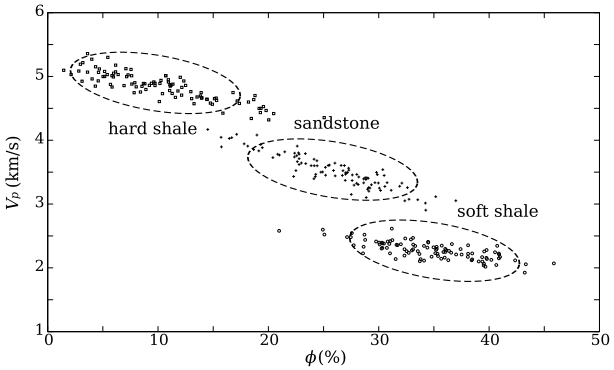

Figure 5. Simulated rock-physics model between porosity ϕ and P-wave velocity V_p. Among three layers, the P-wave velocity depends least on the porosity in the soft shale layer.

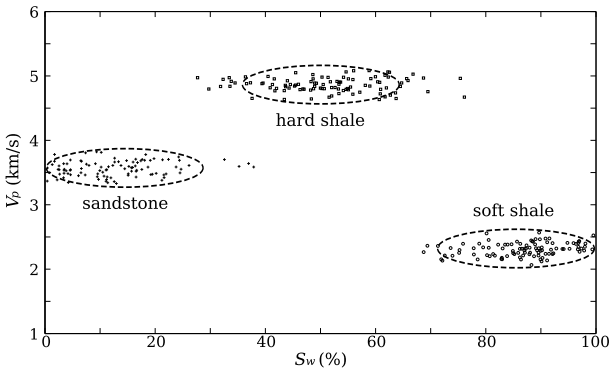

Figure 6. Simulated rock-physics model between water saturation S_w and P-wave velocity V_p. The P-wave velocity depends less on the water saturation than on the porosity.

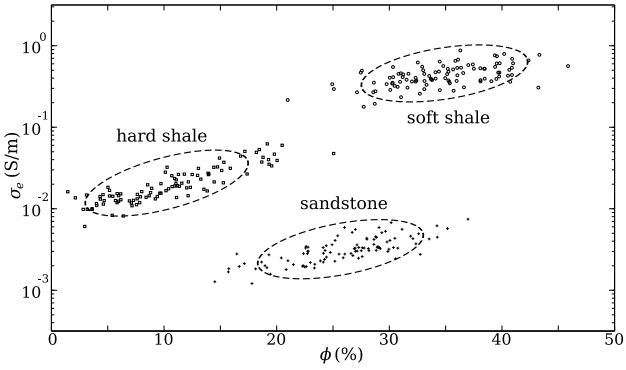

Figure 7. Simulated rock-physics model between porosity ϕ and electric conductivity σ_e. For each layer, increased porosity tends to accompany larger electric conductivity.

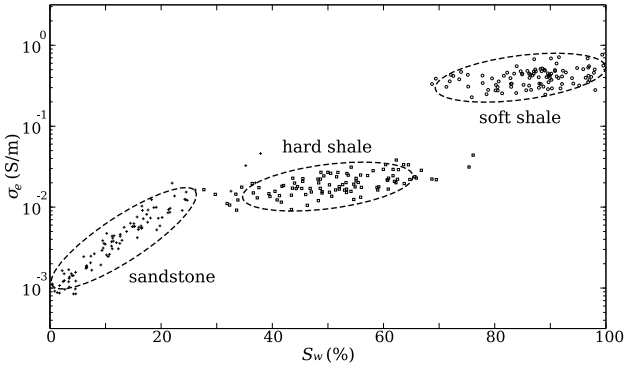

Figure 8. Simulated rock-physics model between water saturation S_w and electric conductivity σ_e. Among three layers, the dependency of the electric conductivity on the water saturation is strongest in the sandstone layer.

lognormal random numbers are thereafter added to the P-wave velocity and electric conductivity, respectively, to account for the uncertainty in rock-physics model. Figures 5 through 8 show the simulated rock-physics models, where the porosity and water saturation samples of each layers are retrieved from the prior distributions. The distributions for the P-wave velocity indicate that the velocity is strongly dependent on the porosity and the contribution of the water saturation is less significant. In contrast, the distributions for the electric conductivity show that both the porosity and water saturation influence the electric conductivity. Note that the dependencies are different for each layer. The dependency of the P-wave velocity on the porosity is weakest in the soft shale layer and the dependency of the electric conductivity on the water saturation is strongest in the sandstone layer. These differential dependencies in the different layers play a significant role in the joint inversion presented in this project.

We assume the likelihoods of the P-wave velocity $f(\mathbf{d}_{V_p}|\mathbf{m}_\phi, \mathbf{m}_{S_w})$ and logarithm of electric conductivity $f(\mathbf{d}_{\sigma_e}|\mathbf{m}_\phi, \mathbf{m}_{S_w})$ to follow the multivariate Gaussian distribution (equation (4)). For the evaluation of the likelihoods, we further assume that the P-wave velocity and electric conductivity of each layer (Figure 4) to be independent. We model the covariance matrices $\mathbf{\Sigma}_{V_p}$ and $\mathbf{\Sigma}_{\sigma_e}$ (Figure 2) as diagonal matrices as shown in equation (5), where the variances $\sigma_i^2(V_p)$ and $\sigma_i^2(\sigma_e)$ are constants.

3.2 Seismic data likelihood modeling

There are many kinds of seismic data we can utilize: reflection data, travel time data, amplitude versus offset or angle data, and full waveform data. The full waveform data is the most general and encapsulates the largest amount of information. Seismic migration is the most common approach for handling the full waveform data to reconstruct subsurface geometry. The application of the full waveform inversion is limited by its poor convergence speed.

We use the waveform data for the joint inversion of seismic and CSEM data, because the Monte Carlo

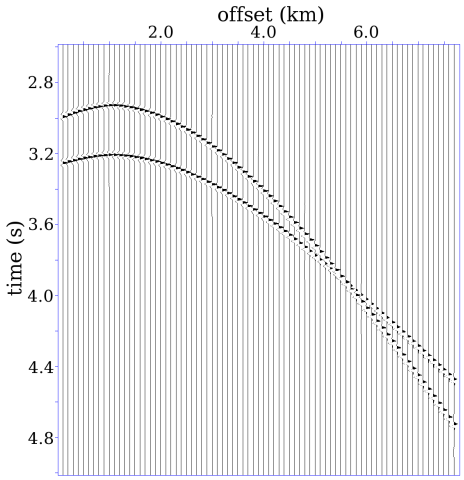

Figure 9. Ray tracing based seismic traces for the 1-D model shown in Figure 4. The modeled reflection events are generated on the top and bottom boundaries of the gas saturated sandstone. The central frequency of the source wavelet is 30 Hz and the time sampling interval is 3 ms.

method is effective for the least-squares misfit optimization for the velocities (Jannane *et al.*, 1989; Snieder *et al.*, 1989). Seismic waveform data is synthesized by a ray-tracing algorithm (Docherty, 1987) and we model the primary reflections of the P-wave from the top and bottom boundaries of the target sandstone layer. Figure 9 shows the representative time traces simulated from the 1-D model shown in Figure 4. Typical reflection parabola and phase shift at post-critical incidence (Aki & Richards, 2002) are observed. In this project, we use the time series data that corresponds to 2 km source-receiver offset and add random noise to the synthesized data.

There are many sources of seismic noise in a marine environment: ambient noise, guided waves, tail-buoy noise, shrimp noise, and side-scattered noise (Yilmaz, 1987). We model the seismic noise by adding band-limited noise as shown in Figure 10. The frequency band of the noise is between 10 and 55 Hz, and the central frequency of the source wavelet is 30 Hz. Figure 11 shows a realization of noisy seismic data that is contaminated by band-limited noise. The maximum amplitude of the noise is 30% of the maximum amplitude of the noise-free signal.

We assume that the seismic data likelihood probability $f(\mathbf{d}_s|\mathbf{d}_{V_p})$ follows the multivariate Gaussian distribution (equation (4)). For the calculation of the likelihood, it is necessary to evaluate the covariance matrix $\mathbf{\Sigma}_s$ (Figure 2). For band-limited noise, the covariance matrix follows from the power spectrum of the band-pass filter and the resulting covariance matrix is not diagonal. We approximate the covariance matrix of a band-limited noise as the covariance matrix of a white

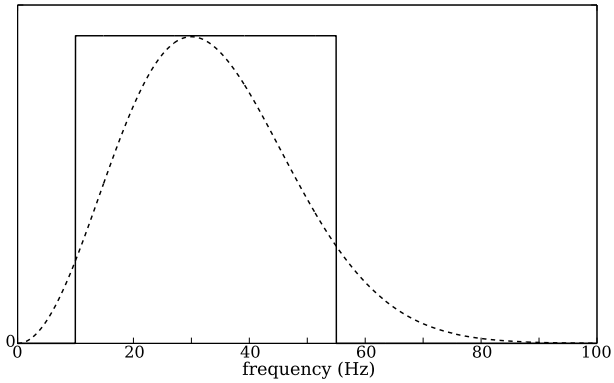

Figure 10. Band-width of the noise (solid line) and amplitude spectrum of the source wavelet (dashed curve). The amplitude spectra are normalized for comparison.

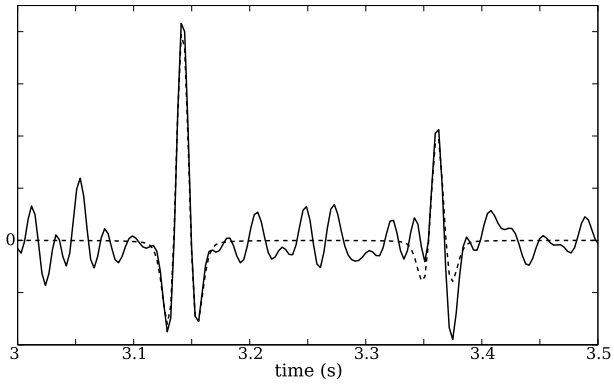

Figure 11. Time trace of a data contaminated by the band-limited white noise (solid curve) and noise free data (dashed curve). The exact P-wave velocities are used for the seismic data calculation shown here.

noise. We therefore model the covariance matrix as a diagonal matrix as shown in equation (5), where the variance values $\sigma_i^2(d_s)$ are identical.

3.3 CSEM data likelihood modeling

The controlled source electo-magnetic (CSEM) method has been studied for the last few decades (Cox *et al.*, 1978) and the feasibility for the delineation of a hydrocarbon reservoir has recently been discussed (Mehta *et al.*, 2005). There are several data acquisition geometries in the CSEM method and horizontal electric dipole transmitter and radial electric field response is generally preferred (Chave & Cox, 1982).

Contrary to seismic wave propagation, EM energy transport within the earth is diffusive and the EM field strength decreases to $1/e$ order in a length called skin depth (Jackson, 1999), defined as

$$\delta = \sqrt{\frac{2}{\mu_m \sigma_e \omega}} \approx 0.503 \sqrt{\frac{1}{\sigma_e f}} \text{ km}, \tag{15}$$

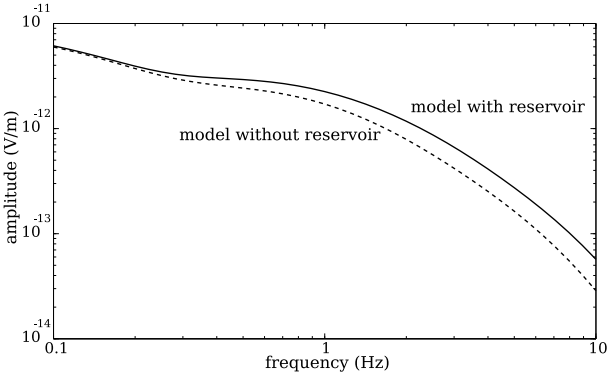

Figure 12. Radial electric field amplitude responses for different frequencies. Transmitter-receiver offset is 2 km. To study the resoving power of the CSEM method detecting the target reservoir, the responses from two models are compared. The model with reservoir is shown in Figure 4 and the model without reservoir is comprised of 1.5 km thick seawater, 1.25 km thick soft shale, and hard shale half-space. The existence of the target sandstone layer is obvious at the high frequency range.

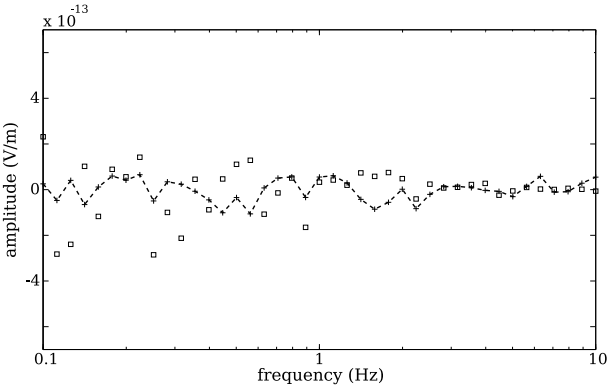

Figure 13. Two different types of CSEM noise: systematic noise (open dots) and non-systematic background noise (dashed curve). The systematic noise decreases with frequency. In contrast, the non-systematic noise is independent of frequency.

where μ_m, σ_e, ω, and f represent magnetic permeability, electric conductivity, angular frequency, and frequency, respectively, all in SI units. For the 1-D model shown in Figure 4, the EM skin depth at 1 Hz is 0.28 km in seawater, 0.8 km in soft shale, 9.2 km in sandstone, and 3.7 km in hard shale layers, respectively. Therefore, about 27 % of the EM field passes through the conductive overburden and diffuses away through the reservoir.

The CSEM signal measured at a receiver location is comprised of three components. The first propagates through the solid earth and contains the information on the reservoir properties. The second propagates through the seawater and attenuates rapidly. It is therefore only significant near the transmitter. The third travels as a

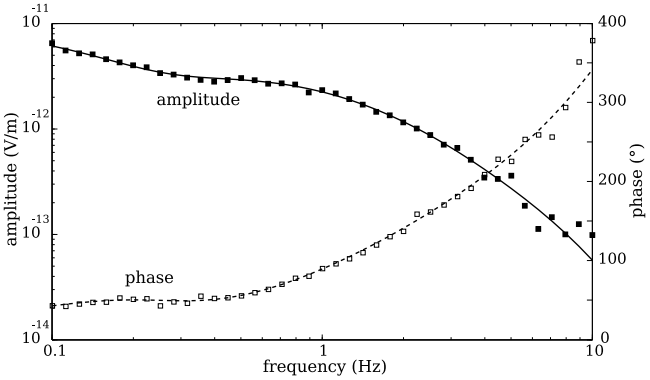

Figure 14. Electric field amplitude and phase response of a noise free (solid and dashed curves) and noise contaminated case (black and open dots). The exact electric conductivities are used for the CSEM data calculation shown here. The CSEM noise is significant in high frequency range.

wave along the seawater-air interface (air-wave). This is independent of the earth geology and diminishes with increasing water depth. In this project, the depth of the sea is 1.5 km and the air-wave is not significant. Figure 12 shows the CSEM response for the different frequencies at 2 km offset. The frequency range is from 0.1 to 10 Hz and the CSEM responses from the two models are compared each other. The difference between the two models is the existence of sandstone layer (target reservoir). The existence of the sandstone layer does not leave an imprint at the low frequency range, because the CSEM response at the low frequency range is sensitive to the deep electric conductivity structure. As we increase the frequency, the discrepancy between the two CSEM responses becomes more significant whereas the signal strength becomes weaker. We choose 2 km transmitter-receiver offset and the frequency range shown in the figure ($0.1 \sim 10$ Hz) for further research.

Even though the deep sub-sea environment has little cultural noise, the CSEM measurements are not entirely free from noise. These noise sources include the magneto-telluric signal, streaming potential, and instrument noise (Constable & Key, 2007). The magneto-telluric signal is significant at frequencies lower than 1 Hz. The streaming potential is generated by seawater movement. The natural background noise at frequencies around 1 Hz is about 1 pV/m (Chave & Cox, 1982) and its influence can be minimized by using a stronger transmitter. The instrument noise is more important and mainly comes from the transmitter amplifier or receiver electrodes. At lower frequency range, the noise from the amplifier and electrodes is proportional to $1/f$ and $1/\sqrt{f}$, respectively. On the other hand, the instrument noise is saturated at the higher frequency range, i.e., Johnson noise limit (Constable & Key, 2007). Furthermore, the CSEM data quality is influenced by positioning error of the transmitter and receiver locations.

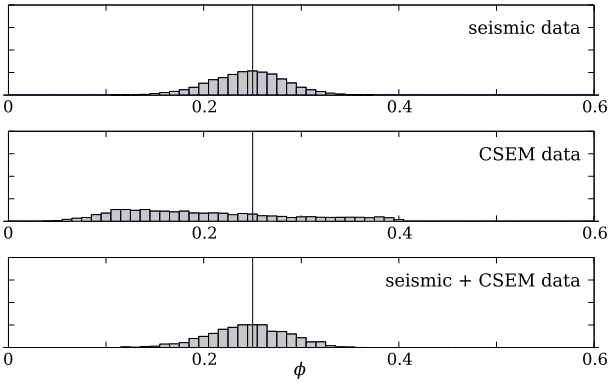

Figure 15. Histograms of posterior porosity (ϕ) samples of the sandstone layer. Vertical line indicates the ground truth value.

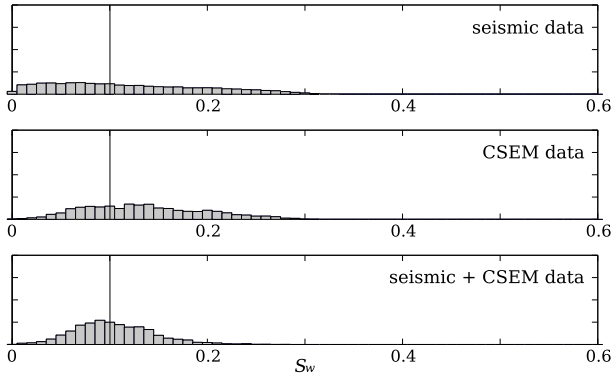

Figure 16. Histograms of posterior water saturation (S_w) samples of the sandstone layer. Vertical line indicates the ground truth value.

The CSEM data we utilize consists of the real and imaginary parts of the CSEM signal. We design the CSEM noise from the amplitude of the CSEM response and then add the noise to the real and imaginary parts of the response. The CSEM noise is categorized as systematic and non-systematic noise as shown in Figure 13. The systematic noise includes the instrument noise and the positioning error. We assume the systematic noise to be proportional to the amplitude of the CSEM signal whereas the non-systematic noise is independent of the signal. A realization of noisy CSEM data is shown in Figure 14, where the systematic noise is 5% of each noise-free amplitude and the non-systematic noise is 5×10^{-14} V/m. The CSEM signal decreases with frequency and the CSEM noise is more obvious.

We assume the CSEM data likelihood probability $f(\mathbf{d}_e|\mathbf{d}_{\sigma_e})$ to follow the multivariate Gaussian distribution (equation (4)). For the calculation of the likelihood, we assume that the CSEM data noise is independent. We model the covariance matrix $\mathbf{\Sigma}_e$ (Figure 2) as a diagonal matrix shown in equation (5). Assuming that the systematic and non-systematic noise are uncorrelated, the diagonal elements of the covariance matrix is derived as

$$\sigma_i^2(d_e) = \sigma_i^2(\varepsilon_{\text{sys}}) + \sigma_i^2(\varepsilon_{\text{nonsys}}), \tag{16}$$

where ε_{sys} and $\varepsilon_{\text{nonsys}}$ denote the systematic and non-systematic noise, respectively. Note that $\sigma_i^2(\varepsilon_{\text{sys}})$ values vary with frequency whereas $\sigma_i^2(\varepsilon_{\text{nonsys}})$ is independent of frequency.

4 UNCERTAINTY ANALYSIS

4.1 Histogram analysis of posterior distributions

We perform MCMC sampling to describe the posterior probability distribution (equation (3)). The random sampling is performed within a six dimensional model space that accounts for porosity or water saturation of soft shale, sandstone, and hard shale layers (Figure 4). The random samples of the porosity and water saturation are retrieved from the posterior probability distribution of three different cases: using seismic data only, CSEM data only, and both seismic and CSEM data. The uncertainty levels applied to the comparison are summarized as the base state variances in Table 3. The posterior distributions of the porosity and water saturation of the target sandstone layer are summarized as histograms as shown in Figures 15 and 16. Note that for the given uncertainties of rock-physics model and data noise levels, the histograms show that the single interpretations weakly constrain porosity and water saturation. However, the histograms from the joint interpretation exhibit a narrower sample distribution of the porosity and water saturation. The figures also show that the seismic data is more sensitive to the porosity than to the water saturation. This is connected with the rock-physics models in Figures 5 and 6 which show that the P-wave velocity has weaker correlation with the water saturation than with porosity. The relatively poor resolution from the CSEM data is attributed to the fact that the sandstone layer is electrically shielded by the more conductive overburden (soft shale layer). These examples illustrate the strength and limitation of both seismic and CSEM methods and explain the motivation of the joint interpretation of seismic and CSEM data. The histograms of the joint interpretation show smaller posterior uncertainty than do the single interpretations. The reduction of uncertainty is more pronounced for the water saturation than for the porosity.

We next compare the histograms that describe the posterior probabilities of different layers. Figure 17 shows the joint posterior distributions of the porosity of three layers. The posterior distribution for the soft shale layer is less constrained than that of the other layers. This is a consequence of the relatively weak correlation between the porosity and P-wave velocity of the soft

type of uncertainty source	base state variance	improved state variance
seismic wave velocity	$(0.1 \text{ km/s})^2$	$(0.03 \text{ km/s})^2$
electric conductivity	$(0.1 \log_{10}(\text{S/m}))^2$	$(0.03 \log_{10}(\text{S/m}))^2$
seismic noise	$(30\% \text{ of max. amplitude})^2$	$(10\% \text{ of max. amplitude})^2$
CSEM noise (systematic)	$(5\% \text{ of each amplitude})^2$	$(2\% \text{ of each amplitude})^2$
CSEM noise (non-systematic)	$(5 \times 10^{-14} \text{ V/m})^2$	$(2 \times 10^{-14} \text{ V/m})^2$

Table 3. Two representative uncertainty levels used in the project. The base states are the uncertainty levels as shown in Figure 5 - 8, Figure 11, and Figure 14.

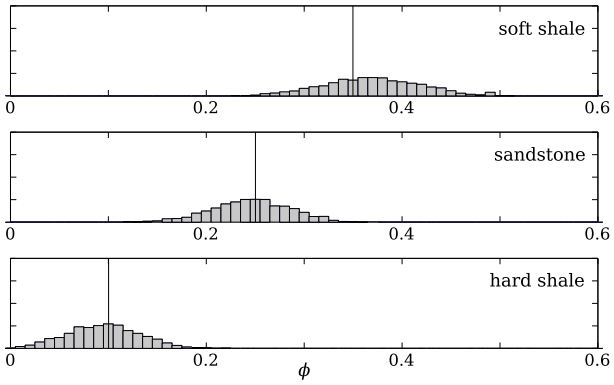

Figure 17. Histograms of posterior porosity (ϕ) samples of the three layers obtained from joint inversion of seismic and CSEM data (base uncertainty level). Vertical lines indicate the ground truth values.

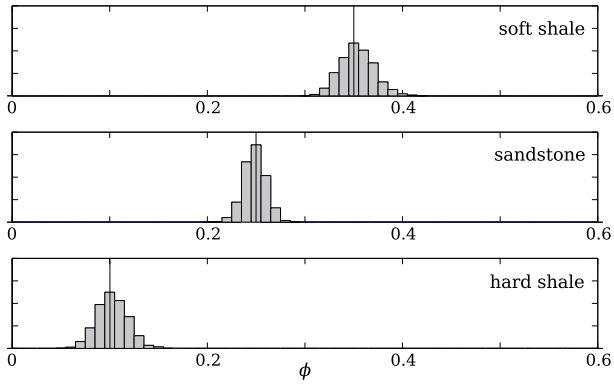

Figure 19. Histograms of posterior porosity (ϕ) samples of the three layers obtained from joint inversion of seismic and CSEM data (improved uncertainty level). Vertical lines indicate the ground truth values.

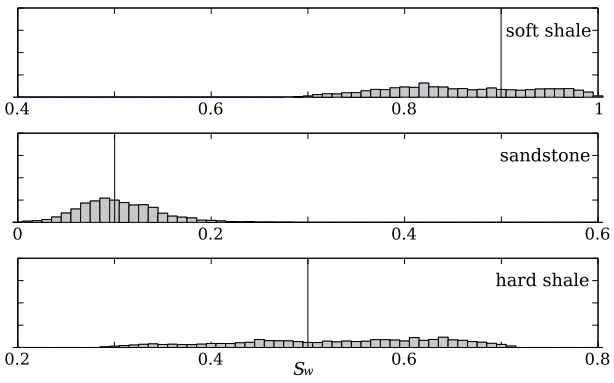

Figure 18. Histograms of posterior water saturation (S_w) samples of the three layers obtained from joint inversion of seismic and CSEM data (base uncertainty level). Vertical lines indicate the ground truth values.

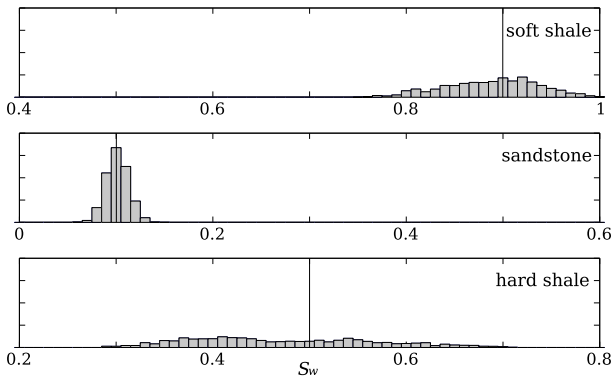

Figure 20. Histograms of posterior water saturation (S_w) samples of the three layers obtained from joint inversion of seismic and CSEM data (improved uncertainty level). Vertical lines indicate the ground truth values.

shale layer (Figure 5). Despite the stronger sensitivity of the seismic and CSEM methods on the properties of the uppermost layer, the weaker correlations of the rock-physics model cause larger variance of the porosity samples. The joint posterior distributions of the water saturation (Figure 18) also exhibit that the posterior distribution for the soft shale layer is less constrained than for the sandstone layer and that the rock-physics model uncertainty has more significance on constraining the posterior distribution than the resolution of the seismic and CSEM methods.

Finally, we study two representative uncertainty levels: a base state and an improved state (Table 3). Note that the uncertainty of the electric conductivity is defined in logarithmic scale. The seismic data uncertainty is defined as a ratio from the maximum ampli-

tude value, and the CSEM data uncertainty is defined as a sum of systematic and non-systematic noise. Figures 17 and 18 represent the posterior probability for the base uncertainty level. The histograms for the improved uncertainty level are shown in Figures 19 and 20. The reduced uncertainty level leads, of course, to a sharper posterior probability distribution than the base state and thus enhances the assessment of porosity and water saturation. This stronger constraint is more obvious for porosity than for water saturation. This is due to the smaller resolution of the CSEM method compared to the seismic method.

4.2 Different scenarios for uncertainty reduction

In the previous section, we presented histograms that characterize the posterior uncertainty. As stated before, we assume the multivariate Gaussian distribution (equation (4)) for the calculation of prior and likelihood. However, there are several factors that make the distribution of the posterior samples non-Gaussian. First, the porosity or water saturation have values between 0 and 1. Second, the porosity sampling is bounded by the critical porosity ϕ_c. The critical porosity is the threshold value between the suspension and the load-bearing domain and denotes the upper porosity limit of the range where the rock-physics model can be applied (Mavko *et al.*, 1998). The critical porosity values we apply for the soft shale, sandstone, and hard shale layer are 0.6, 0.4, and 0.4, respectively. These bounds can lead to skewed sample distributions. If the sample distributions are significantly skewed, another appropriate probability distribution should be applied for the probability assessment of the random samples. In this project, the distributions of the samples shown in Figure 17 through 20 do not display hard bounds or skewed distribution and indicate that the Gaussian distribution is a good approximation. The posterior distributions, however, do not necessarily follow the Gaussian distribution because of the nonlinearity of the forward models. The posterior uncertainty can generally be assessed by sample mean and sample variance. For reasons of clarity, we use the Gaussian curves for the representation of the sample mean and sample variance.

In this project, we model four factors of uncertainty: rock-physics model uncertainties of the P-wave velocity and electric conductivity, and noise of the seismic and CSEM data. The posterior probabilities of the porosity and water saturation for the base and improved uncertainty levels (Table 3) are discussed in the previous section (Figures 17 - 20). We perform the following numerical experiments to quantify the contributions of the four possible sources of uncertainty. The initial simulation is performed based on the base uncertainty level. For the analysis of the contributions of each of the factors on the posterior uncertainties, six subsequent simulations are performed with reduced uncertainty levels of one or two of the four factors of uncertainty. We perform the last simulation based on reduced uncertainty levels of all factors of uncertainty (improved level). These eight numerical experiments are summarized in Table 4. We compare the posterior distributions from different treatments with the base and improved level, and deduce how much a treatment contributes on the overall change of the sample variances. The posterior distributions of the porosity and water saturation are shown in Figures 21 - 26.

	uncertainty of the individual factors
base level	none of the factors are improved
treatment-1	only reducing P-wave velocity uncertainty
treatment-2	only reducing electric conductivity uncertainty
treatment-3	only reducing seismic noise level
treatment-4	only reducing CSEM noise level
treatment-5	reducing P-wave velocity uncertainty and seismic noise level
treatment-6	reducing electric conductivity uncertainty and CSEM noise level
improved level	reducing all of the four uncertainty factors

Table 4. Eight numerical experiments for the analysis of the contributions of four possible factors of uncertainty. Two states of uncertainty for the individual factors are listed in Table 3.

Figures 21 and 22 show the posterior probability distributions for the treatments 1 and 2. When we reduce uncertainty levels of P-wave velocity or electric conductivity the resultant posterior distributions exhibit smaller sample variances than the base level. Furthermore, the sample means generally are closer to the ground truth values as we reduce the individual uncertainty levels. The probability density distribution for porosity of the sandstone layer (Figure 21) reveals that the P-wave velocity uncertainty plays a significant role on the overall uncertainty reduction of the porosity and the contribution of the electric conductivity uncertainty is limited. In contrast, Figure 22 shows that the overall uncertainty variation of the water saturation is more strongly influenced by the uncertainty of the electric conductivity than by the uncertainty of the P-wave velocity. This is consistent with the simulated rock-physics models shown in Figures 5 - 8. From the rock-physics models, we can deduce that the porosity strongly influences both the P-wave velocity and electric conductivity. The rock-physics models also show that the water saturation strongly influences the electric conductivity while its influence on the P-wave velocity is limited.

The posterior probability distributions for the treatments 3 and 4 are shown in Figures 23 and 24. When we reduce the noise levels of the seismic or CSEM data, the improvements of the posterior uncertainties of

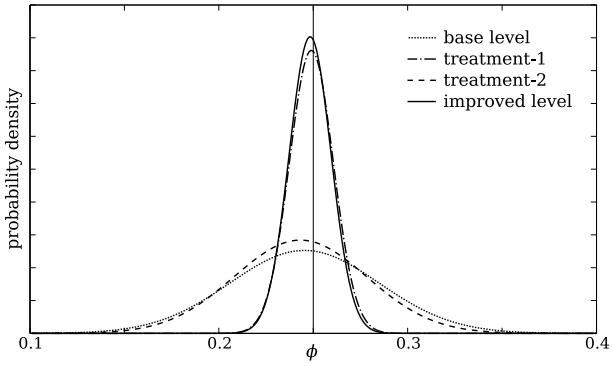

Figure 21. Posterior probability distributions of porosity ϕ of the sandstone layer. The distributions from the treatments 1 and 2 (Table 4) are compared with those from the base and improved levels. Vertical line indicates the true porosity value.

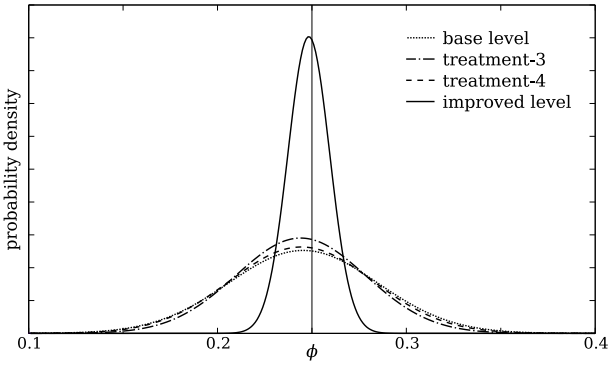

Figure 23. Posterior probability distributions of porosity ϕ of the sandstone layer. The distributions from the treatments 3 and 4 (Table 4) are compared with those from the base and improved levels. Vertical line indicates the true porosity value.

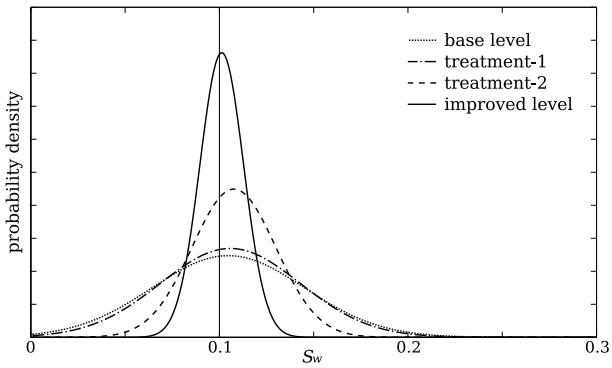

Figure 22. Posterior probability distributions of water saturation S_w of the sandstone layer. The distributions from the treatments 1 and 2 (Table 4) are compared with those from the base and improved levels. Vertical line indicates the true water saturation value.

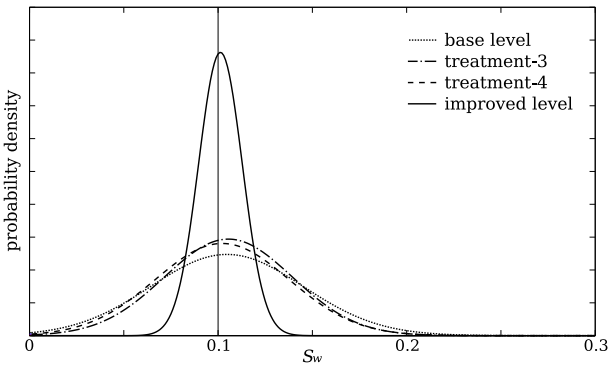

Figure 24. Posterior probability distributions of water saturation S_w of the sandstone layer. The distributions from the treatments 3 and 4 (Table 4) are compared with those from the base and improved levels. Vertical line indicates the true water saturation value.

the porosity and water saturation are much less significant than the improvements due to the reduction of rock-physics model uncertainties. This shows that the overall uncertainty of the porosity and water saturation is more influenced by the rock-physics model uncertainties than by the noise of the seismic or CSEM data. The figures also show that for the given ranges of data noise, the seismic data noise reduction yields a more precise estimate than when the CSEM data noise is reduced.

Figures 25 and 26 show the posterior probability distributions for the treatments 5 and 6. Compared to the single improvement cases, it is clear that the combined improvements give better assessments about the porosity and water saturation. The probability density distributions shown in Figures 25 and 26 exhibit similar distributions as Figures 21 and 22. This implies that the posterior uncertainty variations from the combined improvements are mainly governed by the improvement of rock-physics model uncertainties and the contributions of the seismic and CSEM data noise are less significant.

The posterior probability distributions shown in Figures 21 - 26 are summarized in Table 5. The comparison of the variance values clearly show that the reductions of the sample variances of the porosity and water saturation are most strongly influenced by the uncertainty of the P-wave velocity and electric conductivity, respectively. The contributions of the rock-physics model uncertainties on the posterior uncertainties are generally larger than those of the seismic and CSEM data noise. The numerical experiments suggest different ways of accomplishing uncertainty reduction depending on whether our interests focus on the porosity or water saturation. When the porosity is our prime concern, we can effectively accomplish uncertainty reduction by improved rock-physics model about the P-wave velocity and suppressing the seismic data noise. On the other hand, if we need more accurate assessment about

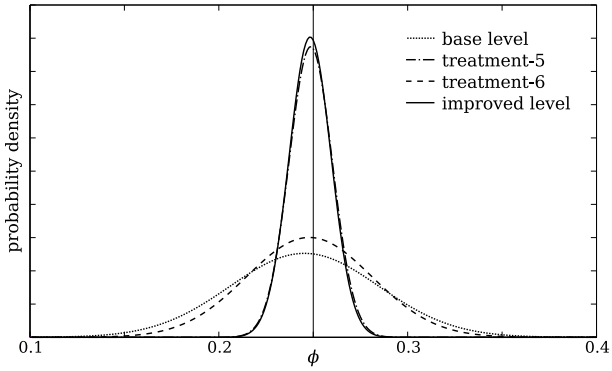

Figure 25. Posterior probability distributions of porosity ϕ of the sandstone layer. The distributions from the treatments 5 and 6 (Table 4) are compared with those from the base and improved levels. Vertical line indicates the true porosity value.

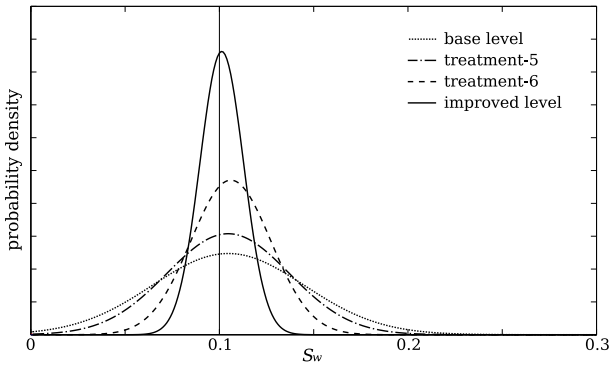

Figure 26. Posterior probability distributions of water saturation S_w of the sandstone layer. The distributions from the treatments 5 and 6 (Table 4) are compared with those from the base and improved levels. Vertical line indicates the true water saturation value.

the water saturation, the acquisition of more detailed electric conductivity information and the suppression of CSEM data noise will be preferred.

5 CONCLUSIONS

We have shown that the posterior probability random sampling based on the Metropolis-Hastings algorithm is capable of assessing the multi-dimensional probability distribution of the porosity and water saturation. We have also shown that the joint inversion of the seismic and CSEM data can be achieved by introducing rock-physics models that interconnect the P-wave velocity and electric conductivity. There are four representative sources of uncertainty that influence the posterior probability density of the porosity and water saturation. These uncertainties are related to seismic wave velocity, electric conductivity, seismic data, and CSEM data.

sample variance ($\times 10^{-3}$)	$S^2(\phi)$	$S^2(S_w)$
base level	1.56	1.63
treatment-1	0.13	1.38
treatment-2	1.24	0.50
treatment-3	1.19	1.16
treatment-4	1.44	1.27
treatment-5	0.13	1.06
treatment-6	1.11	0.45
improved level	0.12	0.13

Table 5. Sample variances S^2 of porosity ϕ and water saturation S_w of the sandstone layer. The details about the treatments are in Table 4.

Even when the single interpretations poorly constrain the posterior distributions of the porosity and water saturation, the distributions from the joint interpretation are well constrained and exhibit reduced uncertainty.

Assuming two levels of overall uncertainty, we study the relative contributions from the four individual sources of uncertainty. The numerical simulations show that rock-physics model uncertainties play a more significant role on the overall uncertainty variation than do seismic and CSEM data noise. The numerical experiment also suggests different ways of accomplishing uncertainty reduction depending on whether our interests focus on porosity or on water saturation. When porosity is our prime concern, we can effectively accomplish uncertainty reduction by acquiring more precise P-wave velocity information and suppressing the seismic data noise. On the other hand, if we need a more accurate assessment of water saturation, the acquisition of more detailed electric conductivity information and the suppression of CSEM data noise are desirable.

It is necessary to emphasize that the conclusions explained above depend on the parameters chosen in this project. Furthermore, there are many sources of uncertainty that we do not take into account such as lithologic variation, variation of mineralogical composition of clay, depth of layers. The methodology of the uncertainty analysis presented in this project can, however, be extended to a specific problem. The employed method can be used for experimental design, and for targeting the source of error that constributes most to the posterior uncertainty.

ACKNOWLEDGMENTS

This work was supported by the Consortium Project on Seismic Inverse Methods for Complex Structures at Center for Wave Phenomena (CWP). We thank Alan D. Chave (Woods Hole Oceanographic Institution) for providing his CSEM code, which was critically important for the success of this study. We acknowledge Inge Myrseth (Norwegian University of Science and Technol-

ogy), Malcolm Sambridge (Australian National University), Albert Tarantola (Institut de Physique du Globe de Paris), Luis Tenorio, Mike Batzle, André Revil, Misac Nabighian, Steve Hill (Colorado School of Mines) for helpful information, discussions, and suggestions. We are also grateful to colleagues of CWP for valuable discussions and technical help.

REFERENCES

Aki, K., & Richards, P. G. 2002. *Quantitative Seismology*. 2nd edn. University Science Books.

Batzle, M., & Wang, Z. 1992. Seismic properties of pore fluids. *Geophysics*, **57**, 1396 – 1408.

Chave, A., & Cox, C. S. 1982. Controlled Electromagnetic Sources for Measuring Electrical Conductivity Beneath the Oceans 1. Forward Problem and Model Study. *Journal of Geophysical Research*, **87**, 5327 – 5338.

Chen, J., Hoversten, G. M., Vasco, D., Rubin, Y., & Hou, Z. 2007. A Bayesian model for gas saturation estimation using marine seismic AVA and CSEM data. *Geophysics*, **72**, WA85 – WA95.

Constable, S., & Key, K. 2007. *Marine Electromagnetic Methods for Hydrocarbon Exploration*. Sociey of Exploration Geophysics.

Cox, C. S., Kroll, N., Pistek, P., & Watson, K. 1978. Electromagnetic Fluctuations Induced by Wind Waves on the Deep-Sea Floor. *Journal of Geophysical Research*, **83**, 431 – 442.

Docherty, P. 1987. *Ray theoretical modeling, migration and inversion in two-and-one-half-dimensional layered acoustic media*. Ph.D. dissertation. Colorado School of Mines.

Gallardo, L. A., & Meju, M. A. 2004. Joint two-dimensional DC resistivity and seismic travel time inversion with cross-gradients constraints. *Journal of Geophysical Research*, **109**, B03311.

Geman, S., & Geman, D. 1984. Stochastic Relaxation, Gibbs distribution, and the Bayesian Restoration of Images. *IEEE Trans on Pattern Analysis and Machine Intelligence*, **6**, 721 – 741.

Gouveia, W. P., & Scales, J. A. 1998. Bayesian seismic waveform inversion: Parameter estimation and uncertainty analysis. *Journal of Geophysical Research*, **103**, 2759 – 2779.

Han, D., & Batzle, M. 2004. Gassmann's equation and fluid-saturation effects on seismic velocities. *Geophysics*, **69**, 398 – 405.

Harris, P., & MacGregor, L. 2006. Determination of reservoir properties from the integration of CSEM, seismic, and well-log data. *First Break*, **24**, 53 – 59.

Hastings, W. K. 1970. Monte Carlo sampling methods using Markov chains and their applications. *Biometrika*, **57**, 97 – 109.

Hoversten, G. M., Cassassuce, F., Gasperikova, E., Newman, G. A., Chen, J., Rubin, Y., Hou, Z., & Vasco, D. 2006. Direct reservoir parameter estimation using joint inversion of marine seismic AVA and CSEM data. *Geophysics*, **71**, C1 – C13.

Jackson, J. D. 1999. *Classical Electrodynamics*. 3rd edn. John Wiley & Sons.

Jannane, M., Beydoun, W., Crase, E., Cao, D., Koren, Z., Landa, E., Mendes, M., Pica, A., Noble, M., Roeth, G., Singh, S., Snieder, S., Tarantola, A., Trezeguet, D., & Xie, M. 1989. Wavelengths of earth structures that can be resolved from seismic reflection data. *Geophysics*, **54**, 906 – 910.

Kaipio, J. P., Kolehmainen, V., Somersalo, E., & Vauhkonen, M. 2000. Statistical inversion and monte Carlo sampling methods in electrical impedance tomography. *Inverse Problems*, **16**, 1487 – 1522.

Mavko, G., Mukerji, T., & Dvorkin, J. 1998. *The Rock Physics Handbook*. Cambridge University Press.

Mehta, K., Nabighian, M. N., Li, Y., & Oldenburg, D. W. 2005. Controlled Source Electromagnetic (CSEM) technique for detection and delineation of hydrocarbon reservoirs: an evaluation. *SEG Expanded Abstract*, **75**, 546 – 549.

Metropolis, N., Rosenbluth, A. W., Rosenbluth, M. N., & Teller, A. H. 1953. Equation of State Calculations by Fast Computing Machines. *The Journal of Chemical Physics*, **21**, 1087 – 1092.

Mosegaard, K., & Sambridge, M. 2002. Monte Carlo analysis of inverse problems. *Inverse Problems*, **18**, R29 – R54.

Mosegaard, K., Singh, S., Snyder, D., & Wagner, H. 1997. Monte Carlo analysis of seismic reflections from Moho and the W reflector. *Journal of Geophysical Research*, **102**, 2969 – 2981.

Musil, M., Maurer, H. R., & Green, A. G. 2003. Discrete tomography and joint inversion for loosely connected or unconnected physical properties: application to crosshole seismic and georadar data sets. *Geophysical Journal International*, **153**, 389 – 402.

Revil, A., Cathles, L. M., & Losh, S. 1998. Electrical conductivity in shaly sands with geophysical applications. *Journal of Geophysical Research*, **103**, 23925 – 23936.

Sambridge, M., Beghein, C., Simons, F. J., & Snieder, R. 2006. How do we understand and visualize uncertainty? *Leading Edge*, **25**, 542 – 546.

Scales, J. A., & Snieder, R. 1997. To Bayes or not to Bayes? *Geophysics*, **62**, 1045 – 1046.

Scales, J. A., & Tenorio, L. 2001. Prior information and uncertainty in inverse problems. *Geophysics*, **66**, 389 – 397.

Sivia, D. S., & Webster, J. R. P. 1998. The Bayesian approach to reflectivity data. *Physica B*, **248**, 327 – 337.

Snieder, R. 1998. The role of nonlinearity in inverse problems. *Inverse Problems*, **14**, 387 – 404.

Snieder, R., Xie, M. Y., Pica, A., & Tarantola, A. 1989. Retrieving both the impedance contrast and background velocity: A global strategy for the seismic reflection problem. *Geophysics*, **54**, 991 – 1000.

Spikes, K., Mukerji, T., Dvorkin, J., & Mavko, G. 2007. Probabilistic seismic inversion based on rock-physics models. *Geophysics*, **72**, R87 – R97.

Tenorio, L. 2001. Statistical Regularization of Inverse Problems. *SIAM Review*, **43**, 347 – 366.

Waxman, M. H., & Smits, L. J. M. 1968. Electrical conductivities in oil-bearing shaly sands. *Society of Petroleum Engineering Journal*, **8**, 107 – 122.

Yilmaz, O. 1987. *Seismic Data Processing*. Sociey of Exploration Geophysics.